

Acoustic Emission Analysis of Damage during Compressive Deformation of Amorphous Zr-Based Foams with Aligned, Elongated Pores

MARIE E. COX and DAVID C. DUNAND

Acoustic emission methods are used to investigate the evolution of internal microfractural damage during uniaxial compression of amorphous Zr-based foams with aligned, elongated pores. The foams are fabricated by means of densifying a blend of crystalline W powders and amorphous Zr-based powders with two oxygen contents (0.078 and 0.144 wt pct) by warm equal channel angular extrusion, followed by dissolution of the elongated W phase from the fully densified amorphous matrix. For the high-oxygen foams, prior powder boundaries in the amorphous struts promote damage that accumulates during compression, resulting in energy-absorbing properties comparable with the low-oxygen foams without stress-concentrating powder boundaries. The influence of pore orientation on the evolution of microfracture damage and the ability of the foams to accumulate damage without catastrophic failure is also investigated: pores oriented from 24 to 68 deg to the loading direction promote wall bending, resulting in foams with more diffuse damage and better energy-absorbing properties.

DOI: 10.1007/s11661-013-1691-1

© The Minerals, Metals & Materials Society and ASM International 2013

I. INTRODUCTION

THE addition of porosity or a ductile secondary phase to brittle bulk metallic glasses (BMGs) has been shown to improve the ductility and fracture plasticity of the foams or composites^[1–6] by inhibiting shear band motion.^[7–14] In addition, the pores or secondary phases produce stress concentrations that can be beneficial to the arrest of shear bands or can promote shear band nucleation and propagation. Tungsten fiber-reinforced Zr-based BMG composites exhibit improved compressive fracture strength and plasticity relative to the monolithic BMGs when fibers are aligned in the direction of loading;^[15] however, when loaded transversely, the tungsten fibers form cracks early in the plastic deformation and effectively stimulate the formation of shear bands in the BMG matrix from stress concentration, reducing the benefits of the secondary phase.^[16] Stress concentrations in low-porosity BMG foams form around pores during loading and can be controlled by pore orientation and geometry. In Pd-based BMG foams with low porosities ($p < 11$ pct), orienting elongated pores perpendicular to the direction of loading increases the stress concentrations induced by the pores and enhances the plasticity of the foam by promoting high densities of interacting shear-bands.^[17] On the other hand, stress concentrations caused by sharp notches in the foam and pores with small radii of

curvature may contribute to premature failure and limited plastic bending, as shown in Ni-based BMG foams ($p = 40$ pct) with highly elongated struts aligned in the direction of compressive loading.^[18]

To improve the ductility of porous BMGs, an understanding of their internal deformation and damage mechanisms is required. Typically, damage mechanisms are identified by observing the sample surface during deformation and imaging fracture surfaces after testing. Despite being useful, these techniques give limited information on the internal damage evolution during testing. Recently, Demetriou *et al.*^[19] studied the yielding of Pd-based BMG foams using real-time, *in situ* X-ray microtomography. This technique demonstrated that percolation of local elastic membrane-buckling instabilities led to nonlinear yielding. Although this method is highly effective, it requires specialized equipment and extensive data analysis. A much simpler and accessible method, acoustic emission (AE), has also been shown to be useful in monitoring the damage evolution in BMG foams.^[20,21] Although this method is not spatially resolved, thus providing only average information on the fracture mechanisms operative during testing, AE activity can be used to track, with high time resolution, the evolution of damage to foams during compression.

Here, we investigate the AE activity of Zr-based BMG foams with aligned, elongated pores, created by removing the W phase from a BMG/W composite consolidated by equal channel angular extrusion (ECAE). Variations in the base amorphous powder's composition resulted in two different amorphous open cell foams characterized by dense cell walls with and without prior powder boundaries. Here, for the first time, AE techniques are used to investigate the influence of prior powder boundaries and

MARIE E. COX, National Research Council Fellow, is with the Naval Research Laboratory, Washington, DC 20001. DAVID C. DUNAND, Professor, is with the Department of Materials Science and Engineering, Northwestern University, Evanston, IL 60208. Contact e-mail: dunand@northwestern.edu

Manuscript submitted September 22, 2012.

Article published online March 20, 2013

pore orientation (with respect to the direction of loading) on the evolution of the internal damage to amorphous foams during compression testing.

II. EXPERIMENTAL PROCEDURES

As described in detail in a previous study,^[5,22] we use here $\text{Zr}_{58.5}\text{Nb}_{2.8}\text{Cu}_{15.6}\text{Ni}_{12.8}\text{Al}_{10.3}$ or $\text{Zr}_{56.3}\text{Nb}_{5.1}\text{Cu}_{15.6}\text{Ni}_{12.9}\text{Al}_{10.0}$ powders (38 to 105 μm , fabricated at the Materials Processing Center of Ames Laboratory by high-pressure gas atomization) with oxygen contents of 0.078 and 0.144 wt pct, respectively, which are referred to as low-oxygen and high-oxygen powders, respectively. The BMG powders were mixed with 60 or 70 vol pct crystalline tungsten powders (from 45 to 106 μm in size), and the blends were sealed into Ni-100 cans which were pushed at rates of 0.13 and 0.5 mm/s (for the high- and low-oxygen content BMG powders, respectively) through a 90 deg ECAE die walls which were heated to 703 K and 693 K (430 °C and 420 °C) (within the BMG's supercooled liquid region), respectively, with no counter-pressure.

After a single pass, consolidated composite compression samples ($\sim 2 \times 2 \times 4 \text{ mm}^3$ for composites made with low-oxygen powders and $\sim 3 \times 3 \times 6 \text{ mm}^3$ for high-oxygen powders) were electrodischarge machined from each can with varying orientations with respect to the main direction of shear during extrusion through the 90 deg die, along which the W powders were elongated.^[23] Low-oxygen composites were machined with the long dimension of the compression sample in the direction of extrusion to produce composites with elongated powders aligned ~ 26 deg to the direction of loading.^[22] High-oxygen composites were machined with elongated powders aligned at angles of ~ 0 , 24, 44, and 68 deg to the long dimension of the sample. High-oxygen samples were also machined with the long dimension perpendicular to both the flow plane and direction of extrusion, resulting in foams with elongated pores at an angle of 90 deg to the direction of loading.^[24]

Removal of the W phase from the composites was achieved by immersing the samples for a duration ranging from 32 to 120 hours in an electrochemical cell with a solution of 1.5M KOH and a voltage of 5 to 5.4 V, and was monitored for the mass loss. Before and after dissolution, samples were coated with a thin layer of vacuum grease and their porosities were determined by the Archimedes method, wherein the samples' masses were measured in air and in water.

Foams were uniaxially compressed under displacement control at a nominal strain rate of $5 \times 10^{-4} \text{ s}^{-1}$ using an MTS servohydraulic universal testing system, with platens pushing on hardened tool steel pistons (with a lubricated steel sleeve ensuring parallelism) in contact with the sample. Stress was recorded as a function of crosshead displacement from which strain was calculated, using load train compliance corrections based on a calibration stress-strain curve measured on an aluminum sample before and after each test.

Acoustic emissions were measured during the compression test by three broadband piezoelectric transducers (Deci Model SE9125-M) coupled with silicone grease, one on each platen and the third fixed to the upper steel piston.^[20] AE events were recorded after pre-amplification (34 dB) using a Vallen AMS5 acoustic emissions test system. The measurement time resolution was 0.1 μs , rearm time was 3.2 ms, and the triggering threshold was 40 dB relative to a 1 μV transducer output before pre-amplification. To minimize attenuation, silicone grease was also applied to both specimen/piston interfaces. To remove acoustic activity originating outside the gauge region, events were filtered using a 2-ms discrimination time to eliminate events first detected on the transducers located on each platen.

III. RESULTS AND DISCUSSION

A. Microstructure

Figures 1(a) and (c) show scanning electron microscopy (SEM) micrographs of foams made using low-oxygen powders (0.078 wt pct oxygen), labeled hereafter as foams L. These foams, with a porosity $p = 59$ to 63 pct, exhibit dense cell walls with no clearly recognizable prior powder boundaries, and evenly distributed, aligned, and elongated pores (from 25 to 150 μm in width and 80 to 350 μm in length in the cross sections) created when the amorphous powders flowed and densified around the elongating W powders during ECAE densification. The resulting structure is a foam composed of dense walls that surround interconnected pores elongated in the direction of shear. For the high-oxygen foam (0.144 wt pct oxygen, labeled hereafter as foams H), the amorphous phase did not fully densify, and the cell walls show prior powder boundaries (Figures 1b, d) resulting in foams with porosities: $p = 37$ –58 pct. This difference is probably due to the higher oxygen content of the powders (0.144 wt pct) reducing the plastic flow necessary for full powder densification, given that the brittleness of amorphous Zr-based alloys increases with oxygen content.^[25] The preferential deformation of the high-oxygen powders in the shear direction is highlighted by the clearly visible powder boundaries that remain after extrusion (Figures 1b, d). The shear stresses imposed on the canned blend of amorphous Zr-based and crystalline W powders as they were extruded through a 90 deg bend resulted in large deformations of the powders in the shear direction. The adjoining amorphous powders that codeform in the shear direction are bonded over a large surface area because of the large deformation and form elongated struts aligned with the W phase (Figure 1b, A). Perpendicular to the shear direction, amorphous powders tend to deform around the W powders undergoing little deformation in directions perpendicular to the shear direction and result in short struts composed of amorphous powders that are bonded over a limited surface area (Figure 1b, B). The resulting structure is a series of struts that are composed of bonded powders. Struts that are formed in the shear direction tend to be

longer and show better bonding characteristics between BMG powders, while struts not aligned in the shear direction tend to be shorter and are not as well bonded as the former.

B. Damage Evolution and Acoustic Emission Analysis

1. Foams with pores with 26 deg orientation

The stress–strain curves for sets of low- and high-oxygen foams with pores oriented ~26 and ~24 deg to the direction of loading (referred to as Foams L-26 and H-24, respectively) are shown in Figures 2a and b, respectively. Both sets of foams have similar compressive behaviors with a drop in stress after yielding and a long plateau region reminiscent of ductile crystalline metallic foams. To track the evolution of acoustic activity during compression testing, the normalized acoustic event count rates were calculated by dividing the average acoustic emissions over a 5 pct strain interval by the average acoustic emissions for the full strain range, taken as 0 pct < ϵ < 75 pct, and plotted for ϵ < 60 pct for plot readability. Both sets of foams have near-constant average count rate, but a small gradual increase in activity is observed as stresses increase over a range from 5 to 15 pct strain and a decrease of activity is observed as the stress decreases. Although the total event count cannot be directly compared between specimens because of differences in samples' porosities

and volumes, a normalized event count provides insight into the overall acoustic activity. Using the mass of the removed W space holders and assuming that each W powder created an individual pore, the total number of acoustic events per pore was calculated to be in the ranges of 0.8 to 1.1 and 0.7 to 1.1 for foams L-26 and H-24, respectively. Therefore, it appears that about one wall per pore in both types of foams experiences, on average, a fracture that creates an acoustic event with an amplitude greater than 40 dB over the strain range tested.

To describe AE activity, the Gutenberg–Richter (GR) relationship^[26] was utilized:

$$\log N(A) = a - b \cdot A \quad [1]$$

where $N(A)$ is the cumulative number of events having an amplitude greater than A , b is the slope of decay, and a is the zero-amplitude intercept that gives the total number of AE events in the population (however, the a value is very sensitive to size effects and acoustic attenuation caused by experimental set up and detector sensitivity). To account for the acoustic events being recorded in decibels rather than in base 10 logarithmic scale, peak amplitude, the b parameter is multiplied by a factor of 20 to produce a modified value, referred to as the AE- b parameter. The GR power-law relationship (Eq. [1]) was fit using AE data of amplitude 40 dB < A < 65 dB to

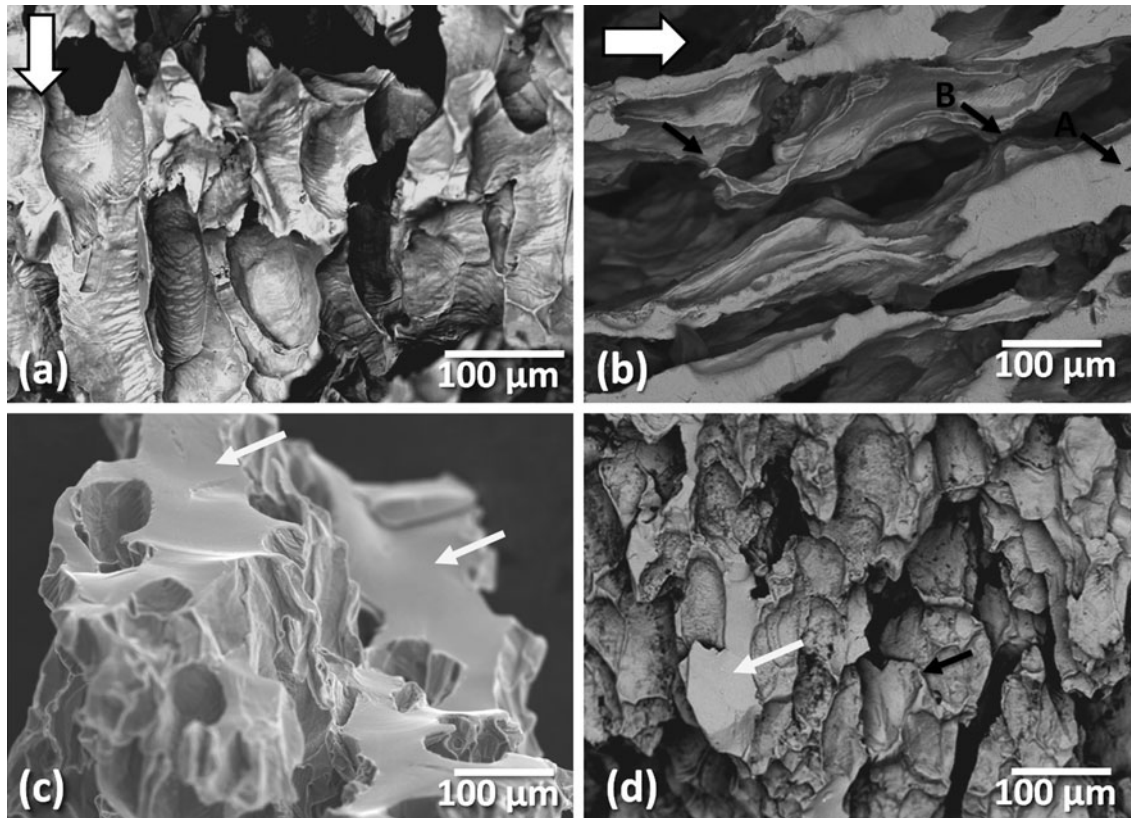


Fig. 1—SEM images of cut surface of (a) low-oxygen foam L-26, (b) high-oxygen foam H-24 samples, with the large white arrows indicating direction of extrusion. SEM images of compressive fracture surface of (c) foam L-26, and (d) foam H-24 samples; the small white arrows indicate flat surfaces indicative of fractures within the metallic structure, whereas the small black arrows indicate prior powder boundaries. An elongated prior powder boundary in the shear direction and a short strut 90 deg to the shear direction are indicated by A and B, respectively.

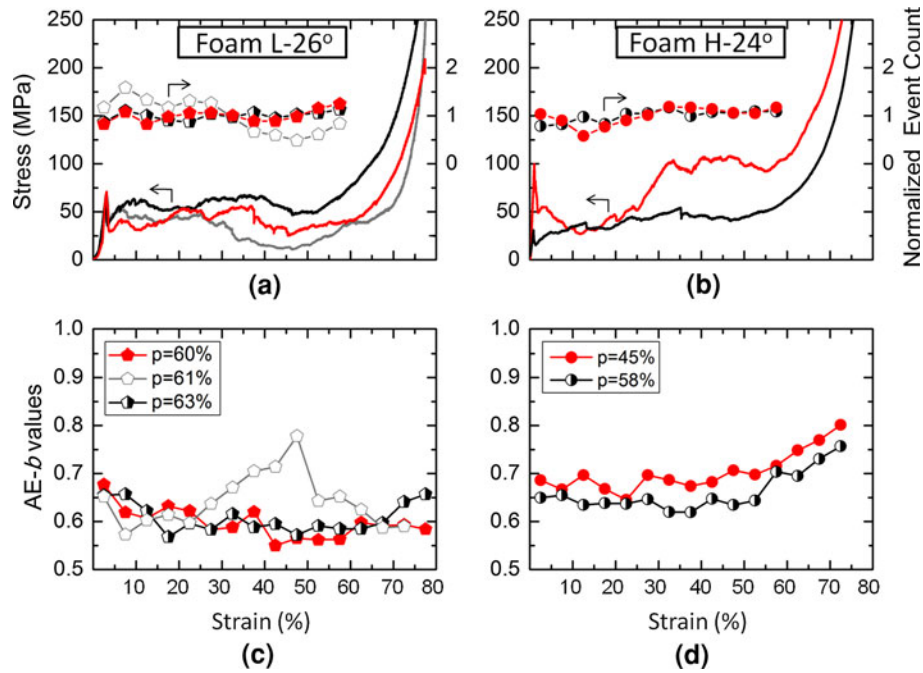


Fig. 2—Compressive stress–strain curves and normalized AE count rates for (a) foam L-26, (b) foam H-24; evolution as a function of compressive strain of parameter AE-*b* (Eq. [1]) characterized over 5 pct strain intervals for (c) foam L-26 (d) foam H-24.

avoid sample size effects; these are reflected by deviations from power-law behaviors at high amplitudes due to high-energy fracture events operating over spatial dimensions comparable with the size of the sample, or events that occur sufficiently close to the sample boundaries which interact with the sample surfaces.^[20,27] The cumulative amplitude distribution for the full AE population (up to 60 pct strain) and the GR power-law fit are shown in Figure 3 for L-26 and H-24 foams.

For a large AE-*b* value, the AE activity decays quickly with increasing amplitude, indicating fewer high-energy events as compared with low-energy events over the amplitude distribution; smaller AE-*b* values reflect AE activity with comparatively more high-energy fractures. As observed in Figure 3, H-24 foams have slightly larger AE-*b* values (0.67 to 0.71) compared with L-26 foams (AE-*b* = 0.59 to 0.64). The larger AE-*b* values reflect that the H-24 foams have more low-energy fractures at the expense of high-energy fractures compared with the L-26 foams, as both had same total number of events per pore. The less-energetic fractures in the H-24 foams may be a result of diffuse microfractures occurring along the prior powder boundaries instead of more localized, high-energy microfractures through solid cell walls. Figure 1d shows the fracture surface of a H-24 foam with cracks propagating through the prior powder boundaries as opposed to the fracture surface seen in Figure 1c that shows crack propagation through solid cell walls in a L-26 foam. The prior powder boundaries probably act as a stress concentrator, weakening struts and producing preferred path for cracks leading to more diffuse low-energy fractures. Similar behavior has been noted in the AE activity of composite BMG/W foams during compression.^[21] The composite foam, with struts

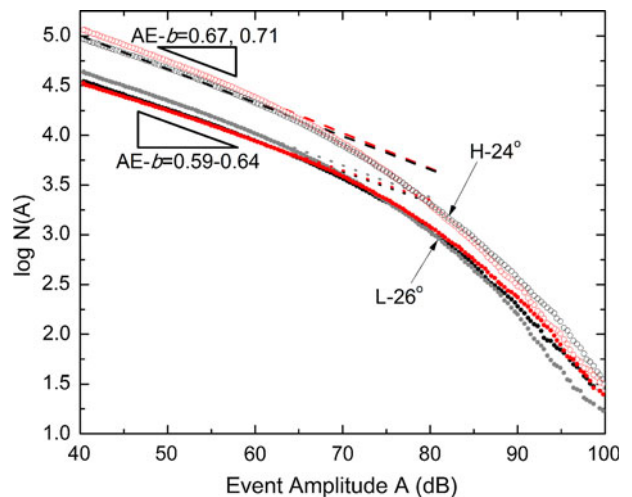


Fig. 3—Logarithmic cumulative acoustic emission amplitude distributions for the full population of acoustic events for foams L-26 and H-24, with slope, AE-*b* parameter (Eq. [1]), labeled.

composed of a Zr-based BMG matrix containing an evenly dispersed W powder second phase, had higher AE-*b* values (full population AE-*b* = 0.84) compared with fully amorphous foams without crystalline W inclusions (full population AE-*b* = 0.42), which was attributed to the dispersed W phase acting as a stress concentrator and location for crack nucleation, creating more diffuse acoustic activity and weaker foams.^[21]

To gain insight into the evolution of the internal microfractural mechanisms, the AE data were separated into subpopulations spanning 5 pct strain intervals, and

the GR parameters were obtained by fitting the cumulative amplitude distribution of each subpopulation as previously described. As expected from the full population AE- b values, the evolution of these partial population AE- b values for L-26 foams are consistently lower than those for the H-24 foams (Figures 2c and d). The L-26 foams, with fully bonded cell walls, show a decrease in AE- b values after yielding: one explanation for this behavior is that, during yielding, evenly distributed weak cell walls fail and transfer load to the thicker walls which subsequently lead to a more localized fracture. For foam L-26, localized high-energy fractures are recorded between 5 and 9 pct strains which correspond to the formation of the first visible surface crack (macro-fracture) forming a 22 through 28 deg angle with respect to the direction of loading (*i.e.*, in the shear plane). By 10 through 15 pct strain, the crack had propagated through the width of the sample to form a through-crack observable without magnification.^[24] The lowest AE- b values observed between 5 and 20 pct strains probably correspond to a number of internal and surface cracks linking up within a shear plane; this creates high-energy fractures which form a macroscopic through-crack spanning the width of the sample. Small fluctuations in AE- b values between 25 and 60 pct strains are observed for two of the L-26 pct foams (with $p = 60$ and 63 pct, referred to as foams L-26/60 pct and L-26/63 pct). These fluctuations in AE- b values correspond to drops in stress that are likely due to the formation of internal and surface cracks that continue to form parallel to the initial crack (at 26 deg to the direction of loading). During foam densification at the highest strain, there is a small increase in AE- b values which is related to the effects of confinement.^[20] In contrast to the two foams L-26/60 pct and L-26/63 pct, the AE- b values for the third foam L-26/61 pct shows a considerable increase in the AE- b values starting around 25 pct strain, peaking at AE- $b = 0.8$ at 45 pct strain, and decreasing to AE- $b = 0.6$ at 65 pct strain. This increase in diffuse damage is accompanied by a dip in both the stress and the normalized AE count rate. This behavior can be explained by assuming that most of the struts, both strong and weak, fractured at low strains, as captured by the localized, high-energy activity recorded. The highly localized damage at low strains, possibly caused by a defect in the foam, leads to very diffuse damage and low stresses at higher strains because a relatively small number of weak struts remained load bearing.

In contrast to the L-26 pct foams, the H-24 pct foams show a relatively constant AE- b value from initial loading to densification (Figure 2d). The small fluctuations in AE- b ranging from 0.65 to 0.7 indicate that the microfractural damage within the foams remains constant during compression and that the crack formation and propagation produce acoustic events throughout the compression curve, which are very similar. This is probably due to the evenly distributed prior powder boundaries which guide the path of the cracks producing diffuse lower-energy events at their location, compared with the more localized events caused by the fracture of solid cell wall.

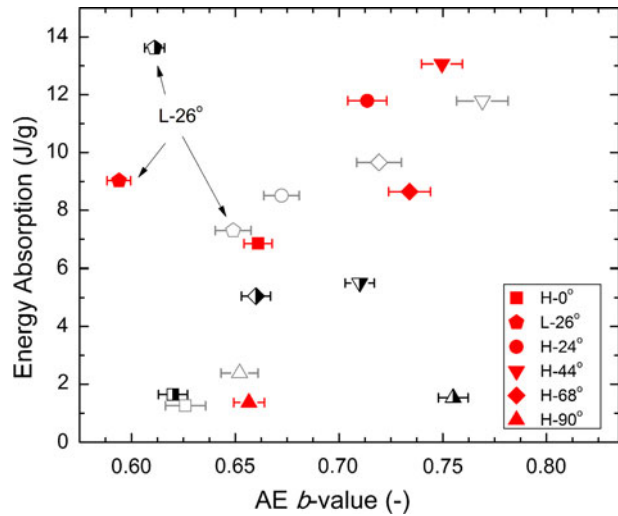


Fig. 4—Energy absorbed during compressive deformation of low-oxygen foams L-26 and high-oxygen foams H-0, H-24, H-44, H-68, and H-90 as a function of AE- b parameter (Eq. [1]).

Although the fracture behaviors differ between the L-26 and H-24 foams, the latter foams also form a visible primary crack along the shear plane, 24 deg to the direction of loading, ranging from ~4 to 8 pct strain and exhibit many secondary cracks being formed parallel to the primary crack as the strain increases.^[24] The L-26 and H-24 foams have similar energy-absorption capabilities despite their different structures. Figure 4 shows AE- b values obtained for the full population distributions (as shown in Figure 3) vs the energy absorption per foam unit mass (calculated using the area under the curve for $\epsilon < 60$ pct divided by the foam density) for both L-26 and H-24 foams. A possible explanation for the similar values is that the prior powder boundaries in the H-24 foams guide the crack growth through a more tortuous path, creating more diffuse damage as fractures between weakly bonded powders release lower energies; this results in foams with similar energy-absorbing capabilities as those with dense cell walls that fracture at more localized locations with higher energies.

2. Foams with pores aligned to the loading direction (0 deg orientation)

The acoustic activity and stress-strain curves of high-oxygen foams with their elongated struts parallel to the direction of loading, referred to as foams H-0, are shown in Figure 5a. These foams were loaded parallel to the well-densified elongated struts aligned in the ECAE shear direction, leading to high foam strengths because most of the struts are load-bearing in compression rather than bending. Despite the high yield strengths, the foams have relatively low AE- b values (0.55 to 0.60, Figure 5b) suggesting localized high-energy fractures. The high normalized count rates and SEM images of fracture surfaces^[24] suggest that many of the struts perpendicular to applied stress, which are subjected to tensile strains because of the Poisson's effect, fractured during loading. As previously discussed, these perpendicular struts tend to be short and composed of powders that are less well

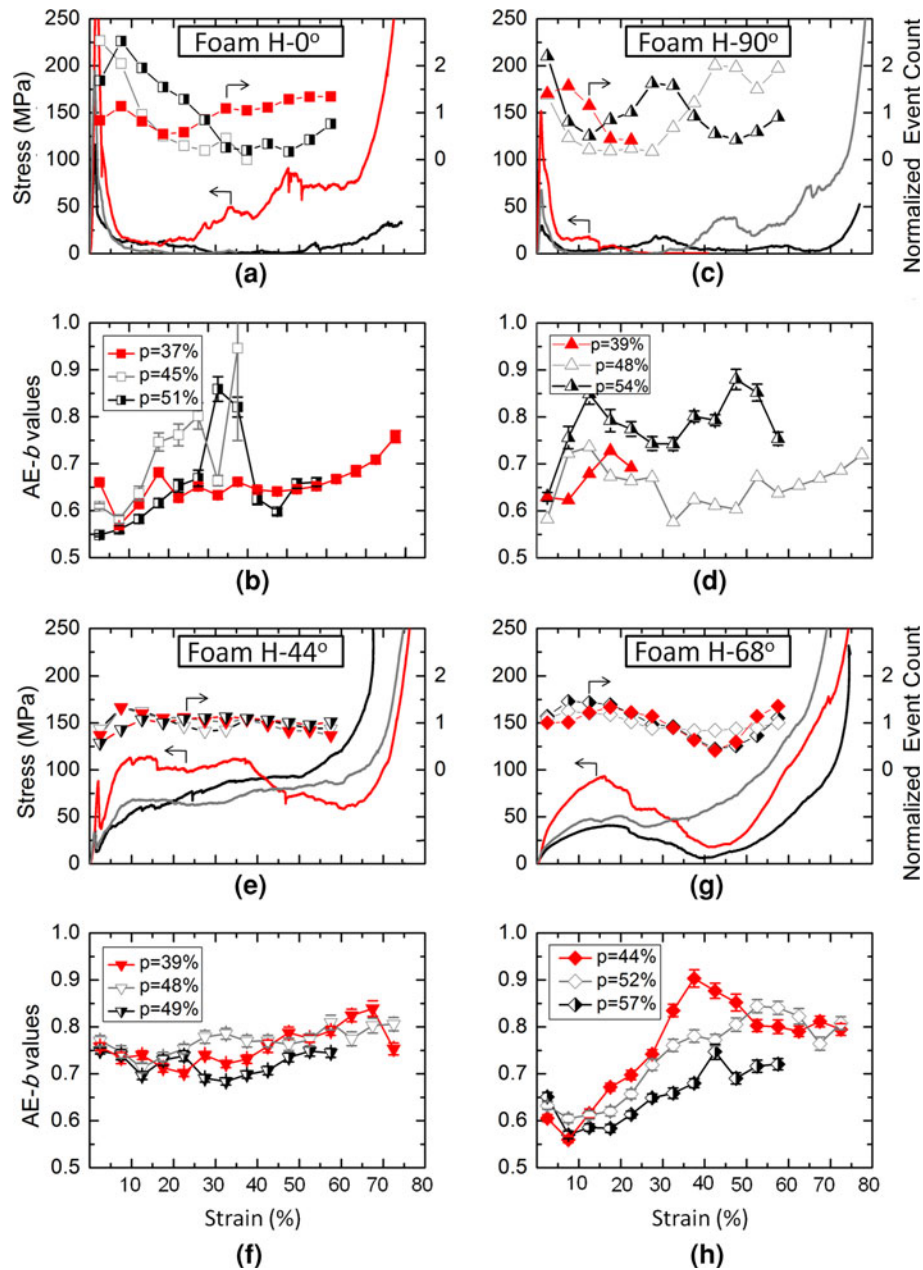


Fig. 5—Compressive stress–strain curves and normalized AE count rates for high oxygen foams (a) H-0, (c) H-90, (e) H-44, and (g) H-68; corresponding evolution of the parameter AE-*b* (Eq. [1]), characterized over 5 pct strain intervals for foams (b) H-0, (d) H-90, (f) H-44, and (h) H-68.

bonded because of reduced deformation outside of the shear direction. The AE activity recorded during loading of foams H-0 is most likely dominated by the microfracture of these weaker perpendicular struts by failure along prior powder boundaries. After yielding, the foams show a very large stress drop and develop many visible vertical cracks that span the whole height of the sample and lead to their vertical splitting.^[24] Large normalized event count rates and high-energy events corresponding to low AE-*b* values (~ 0.57) were recorded. The acoustic activity and crack formation beyond the stress drop were most likely due to microfractures in the remaining strong struts perpendicular to the direction of loading. As the

strain increased, more visible cracks form and large portions of the foam split from the sample until little or no load was supported. For foam 0/45 pct and 0/51 pct, the continued formation of large cracks visible to the naked eye, despite a decrease in count rate to nearly zero and an increase in AE-*b* values, can be rationalized by assuming that most of the strong struts fractured during the foam yielding, leaving fewer struts more evenly distributed throughout the sample leading to more diffuse damage. Also, the large portions of the foam that fractured and fell away from the bulk reduce the volume of loaded material, thereby reducing the number of fractures that could occur.

The smaller fluctuations in the total count rate and the AE-*b* values recorded over the strain range of foam H-0/37 pct may be attributed to its significantly lower porosity compared with the other two H-0 foams and the associated thicker struts oriented in the direction of loading as well as the thicker and/or more numerous struts perpendicular to the direction of loading. Although this foam formed cracks during compression, less material disconnected from the bulk of the sample because of the increased connectivity in the material. After yielding, there was an acoustic activity plateau (AE-*b* ~0.65 and normalized count rate ~1.25) corresponding to continuous crack formation and propagation by fracturing weaker struts without unloading significant portions of the sample. As seen in Figure 4, the additional support leads to a higher relative energy absorption (6.8 J/g) and a larger full population AE-*b* value (0.66) compared with the 0/41 pct and 0/51 pct foams (1.2 to 1.6 J/g and ~0.62).

3. Foams with pores perpendicular to the load (90 deg orientation)

Like the previously described foams with their elongated struts parallel to the loading direction, high-oxygen foams with long struts oriented perpendicular to the loading direction are characterized by a rapid increase in stress until yield, followed by a large drop in stress to a long plateau at low stresses (Figure 5c). These H-90 foams also show large fluctuations in both the normalized AE count rate and AE-*b* values (Figure 5d) during compression, as previously observed in the 0 foams (Figures 5a and b). During loading of the H-90 foams, the weak short struts, both parallel and perpendicular to the direction of loading, most probably fracture along powder boundaries.^[24] This is reflected in the AE activity by a high normalized count rate (1.5 to 2.2) and relatively low AE-*b* values (0.58 to 0.63). After yielding, the count rate and the stress decrease while the AE-*b* values increase as large cracks form. The reduction in AE activity is most likely due to the unloading of large portions of the sample, as fragments fracture and separate from the sample and weaker struts fracture at lower loads and lower energies.

4. Foams with pores with 44 deg orientation

The AE activities of the high-oxygen foams with 44 deg wall orientation (Figures 5e and f) were similar to those of the H-24 foams (Figures 2b and d). After loading, there is a drop in stress followed by a rapid reloading to a plateau stress, which is greater than the foams' yield stress. After the post-yield stress drop, there is a slight decrease in the AE-*b* values and an increase in the normalized AE count rate corresponding to the formation of a visible crack at ~44 deg to the direction of loading.^[24] This is consistent with microfractures, which initially formed throughout the sample within shear planes, linking up at ~10 pct strain and creating more localized, high-energy events. As the strain increased, visible secondary cracks parallel to the primary crack were formed and macroscopic shear of the sample was observed at high strains. The slightly higher full-population AE-*b* values for the H-44 foams

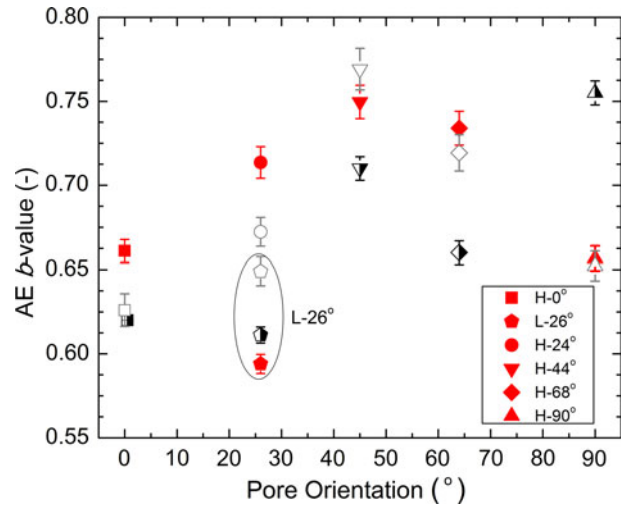


Fig. 6—The parameter AE-*b* (Eq. [1]) as a function of pore orientation for low-oxygen foam L-26 and high-oxygen foams H-0, H-24, H-44, H-68, and H-90.

(AE-*b* = 0.71 to 0.77) reflect more diffuse damage than observed in the H-24 foams (Figure 6). Fracture surfaces of the H-44 foams reveal that many cracks propagated through prior powder boundaries. These cracks tend to be longer than those observed in the 0, 26 and 90 foams which were formed between powders that deformed perpendicular to the direction of shear during extrusion.^[24] The expected increase in bending for the struts oriented 44 deg with respect to the loading direction probably lead to visual observations of plastic deformation in the sample and crack propagation through elongated powder boundaries, resulting in more diffuse damage that accumulated at a steady rate during compression. The H-44 foams displayed the largest relative energy-absorption capabilities (5.5 to 11.7 J/g), which can be attributed to the diffuse low-energy fractures (AE-*b* > 0.71) that accumulated without failure (Figure 4).

5. Foams with pores with 68 deg orientation

The high-oxygen foams with struts oriented ~68 deg to the direction of loading have a distinctive stress-strain curve and acoustic activity (Figures 5g and h) compared with the foams with other pore orientations. During initial loading of H-68 foams, the AE-*b* values range from 0.6 to 0.65 and after yielding quickly drop to 0.55 to 0.6, with an increase in count rate corresponding to the formation of a visible crack and crush band at ~68 deg to the direction of loading.^[24] Unlike the other orientations, there was no drop in stress after yielding; instead, the stress continued to increase until ~15 pct strain beyond which it gradually decreased until the start of foam densification at ~45 pct strain. The steady increase in stress after yielding was accompanied by a growing macroscopic crush band formed under the primary crack oriented ~68 pct to the direction of loading. With increasing strain, the crush band began to spall, leading to a gradual decrease in stress and a steady increase in AE-*b* values (peaking at 0.75 to 0.9) and a

decrease in count rates. The relatively large AE-*b* values (full population AE-*b* = 0.66 to 0.73) indicate diffuse damage that likely corresponds to the fracturing of struts along powder boundaries within the crush band. As previously reported,^[24] SEM images of fracture surfaces show plastic deformation and shear-band formation in individual powders. One explanation is that the bending forces on the elongated struts cause sizable plastic deformation in the struts, which is accommodated by shear bands that lead to plastic deformation within individual powders and the formation of cracks that propagate through prior powder boundaries. As the elongated struts continue to bend, fractures at prior powder boundaries propagated and individual powders separated from the foam struts, resulting in the formation of a crush band that spalls at higher strains. Like the H-44 foams, the diffuse damage accumulated without catastrophic failure in these the H-68 foams resulted in medium to high energy-absorption capacities of 5.1 to 9.5 J/g (Figure 4).

6. Overview of pore orientation

Varying the loading direction with respect to the elongated pore orientation has a significant effect on the mechanical properties of the high-oxygen foams. An increase in plastic deformation by bending of struts and cracking between prior powder boundaries occur for foams whose pores form a 24 through 68 deg angle with respect to the direction of loading, leading to larger macroscopic compressive ductility and energy absorption. The larger full-population AE-*b* values for foams with pores with 26 through 68 deg pore orientation (Figure 6) reflect a more diffuse damage consisting of more low-energy events than the foams with pores oriented parallel and perpendicular to the direction of loading. In a previous study of Zr-based foams with elongated pores forming a 44 deg angle with respect to the direction of loading, the fracture surfaces showed evidence of wall plastic bending which was accommodated by cracks propagating along tortuous prior powder boundaries running parallel to the shear direction, as well as microfracture within powders.^[24] Pore orientations that promote the bending in the foam struts therefore promote diffuse, low-energy microfracture damage and allow the foams to accumulate damage without catastrophic failure in compression.

IV. CONCLUSIONS

Equal channel angular extrusion was used to consolidate a blend of W space-holder powders and Zr-based bulk metallic glass powders ($Zr_{58.5}Nb_{2.8}Cu_{15.6}Ni_{12.8}Al_{10.3}$ with 0.078 wt pct O and $Zr_{56.3}Nb_{5.1}Cu_{15.6}Ni_{12.9}Al_{10.0}$ with 0.144 wt pct O). The tungsten phase was electrochemically removed from the densified composites, resulting in foams with highly elongated and aligned pores and open porosity ranging from 35 to 60 pct. Compressive stress strain curves for foams with their pores oriented at various angles with respect to the applied load are quasi-ductile: they exhibit a peak stress, followed by a stress drop and long plateau regions,

terminated by a raise in stress corresponding to foam densification. Depending on pore orientation, foams have a wide range of compressive energy-absorption capabilities (from 1 to 14 J/g) that are related to internal microfractural damages accumulating during deformation, as determined by acoustic monitoring. The presence of prior powder boundaries in the high-oxygen foams can create stress concentrators that influence the path of the fractures, resulting in more diffuse damage; this leads to energy-absorbing properties comparable with stronger foams without prior powder boundaries. The high-oxygen foams with prior powder boundaries show a clear trend: as the acoustic emission parameters AE-*b* increase, higher diffuse damage results in larger energy-absorbing capabilities with maximum values for pore orientations (from 24 to 68 deg to the direction of loading) that promote bending.

ACKNOWLEDGMENTS

MEC was supported by a National Science Foundation Graduate Research Fellowship. This research was partially funded by the Army Research Laboratory (ARL); the authors thank Dr. Suveen Mathaudhu (ARL, currently Army Research Office) for providing the L-26 samples and for helping to develop this project. The authors also thank Dr. Laszlo Kecskes (ARL) for many useful discussions, Mr. Micah Gallagher (ARL) for assistance in machining samples, Mr. Larry Jones (Ames National Laboratory, Department of Energy) for BMG powder and canning preparation; they acknowledge useful discussions with, and use of the ECAE equipment belonging to, Prof. K. Ted Hartwig (Texas A&M University, TAMU) as well as the experimental assistance of Mr. Robert Barber and Mr. David Foley (TAMU) in operating the equipment. The authors finally thank the Infrastructure Technology Institute at Northwestern University for providing access to their acoustic equipment.

REFERENCES

1. D.C. Hofmann, J.-Y. Suh, A. Wiest, G. Duan, M.-L. Lind, M.D. Demetriou, and W.L. Johnson: *Nature*, 2008, vol. 451, pp. 1085–89.
2. H. Choi-Yim, R. Busch, U. Koster, and W.L. Johnson: *Acta Mater.*, 1999, vol. 47, pp. 2455–62.
3. H. Choi-Yim and W.L. Johnson: *Appl. Phys. Lett.*, 1997, vol. 71, pp. 3808–10.
4. C. Fan, R.T. Ott, and T.C. Hufnagel: *Appl. Phys. Lett.*, 2002, vol. 81, p. 1020.
5. S.N. Mathaudhu, K. Ted Hartwig, and I. Karaman: *J. Non-Cryst. Solids*, 2007, vol. 353, pp. 185–93.
6. G. Kumar, A. Desai, and J. Schroers: *Adv. Mater.*, 2011, vol. 23, pp. 461–76.
7. A.H. Brothers and D.C. Dunand: *Adv. Mater.*, 2005, vol. 17, pp. 484–86.
8. C.A. Schuh, T.C. Hufnagel, and U. Ramamurty: *Acta Mater.*, 2007, vol. 55, pp. 4067–4109.
9. A.H. Brothers and D.C. Dunand: *Scripta Mater.*, 2006, vol. 54, pp. 513–20.
10. A. Inoue, T. Wada, X.M. Wang, and A.L. Greer: *Mater. Sci. Eng. A*, 2006, vol. 442, pp. 233–42.

11. M.D. Demetriou, J.P. Schramm, C. Veazey, W.L. Johnson, J.C. Hanan, and N.B. Phelps: *Appl. Phys. Lett.*, 2007, vol. 91, p. 161903.
12. A.H. Brothers, D.C. Dunand, Q. Zheng, and J. Xu: *J. Appl. Phys.*, 2007, vol. 102, p. 023508.
13. A. Brothers and D. Dunand: *MRS Bull.*, 2007, vol. 32, pp. 639–43.
14. A.H. Brothers and D.C. Dunand: *Acta Mater.*, 2005, vol. 53, pp. 4427–40.
15. H. Zhang, Z. Zhang, Z. Wang, K. Qiu, H. Zhang, and Q. Zang: *Metall. Mater. Trans. A*, 2006, vol. 37A, pp. 2459–69.
16. H. Zhang, L. Liu, Z. Zhang, K. Qiu, X. Pan, H. Zhang, and Z. Wang: *J. Mater. Res.*, 2006, vol. 21, pp. 1375–84.
17. T. Wada, M. Kinaka, and A. Inoue: *J. Mater. Res.*, 2006, vol. 21, pp. 1041–47.
18. M.H. Lee and D.J. Sordelet: *Appl. Phys. Lett.*, 2006, vol. 89, p. 021921.
19. M.D. Demetriou, J.C. Hanan, C. Veazey, M. Di Michiel, N. Lenoir, E. Üstündag, and W.L. Johnson: *Adv. Mater.*, 2007, vol. 19, pp. 1957–62.
20. A.H. Brothers, D.W. Prine, and D.C. Dunand: *Intermetallics*, 2006, vol. 14, pp. 857–65.
21. A.H. Brothers, B. Mangrich, M. Cox, and D.C. Dunand: *Scripta Mater.*, 2011, vol. 64, pp. 1031–34.
22. M.E. Cox, S.N. Mathaudhu, K.T. Hartwig, and D.C. Dunand: *Metall. Mater. Trans. A*, 2009, vol. 41A, pp. 1706–13.
23. V.M. Segal: *Mater. Sci. Eng. A*, 1995, vol. 197, pp. 157–64.
24. M.E. Cox and D.C. Dunand: *Acta Mater.*, 2013, in review.
25. Y. Kawamura, H. Kato, A. Inoue, and T. Masumoto: *Int. J. Powder Metall.*, 1997, vol. 33, pp. 50–61.
26. B. Gutenberg and C.F. Richter: *Bull. Seismol. Soc. Am.*, 1942, vol. 32, p. 163.
27. J. Aue and J.T.M. De Hosson: *J. Mater. Sci.*, 1998, vol. 33, pp. 5455–62.